A Novel Compact Fiber Optic Concentration Sensing System Based on Machine Learning Demodulation

Jie Xue [ID], Lilong Zhao [ID], Tutao Wang [ID], Lijiang Zhao [ID], and Fenping Cui [ID]

Abstract—A novel compact optical fiber concentration sensing system based on machine learning was proposed and experimentally demonstrated in this paper. The Michelson interferometer (MI) was realized by multiple arc discharge performed on the end of a section of bent bare single-mode fiber (SMF). To improve the stability and accuracy of demodulation, machine learning based on long short-term memory (LSTM) was employed and it provided an accuracy of 97.5%, which is more stable and accurate than conventional peak wavelength tracking due to the fact that LSTM can avoid the effects of dip selection, wavelength sampling rate and spectral noise on the peak wavelength tracking. Furthermore, the proposed sensing system has the advantages of compact size, low cost, high robustness, and ease of fabrication.

Index Terms—Concentration sensing, fiber optic Michelson interferometer, machine learning.

I. Introduction

CONCENTRATION is an essential parameter to characterize the liquid properties of the medium. Accurate measurement of solution concentration is particularly crucial in industrial fields such as petroleum [1], chemical [2], metallurgical [3], and pharmaceuticals [4], where it plays a key role in ensuring and improving product quality. Consequently, developing accurate methods for measuring solution concentration has become a hot research topic.

Traditional methods, such as refractometry and the cyclotron method, have been used to measure concentration. Abbe refractometry [5], for instance, is a contact measurement with a limited range that cannot achieve real-time online monitoring. The cyclotron method [6] is only applicable to substances with rotational properties, and prolonged operation can result in a decrease in the sensitivity of the human eye to the field of view, resulting in large errors. Despite researchers' relentless efforts

Jie Xue, Lilong Zhao, and Fenping Cui are with the Nanjing University of Information Science and Technology, Nanjing 210044, China (e-mail: 2893344969@qq.com; llzhao@nuist.edu.cn; cuifenping@nuist.edu.cn).

Tutao Wang and Lijiang Zhao are with the Jiangsu Key Laboratory for Optoelectronic Detection of Atmosphere and Ocean, Nanjing University of Information Science and Technology, Nanjing 210044, China (e-mail: 1920765116@qq.com; 2418533277@qq.com).

to enhance the performance of these instruments and methods, no substantial breakthroughs have been achieved thus far, primarily due to the inherent limitations of traditional experimental approaches.

Compared with conventional approaches, optical fiber sensors have attracted increased research interests due to their advantages including compact structures, exceptional sensitivity, resistance to corrosion, and immunity to electromagnetic interference. In recent years, a number of fiber optic sensors for concentration measurement based on fiber Bragg grating (FBG) [10], [11], [12] and surface plasmon resonance (SPR) [13], [14], [15] have been reported. For example, Wu et al. achieved high accuracy in concentration measurement by detecting hydroacoustic signals generated by the photoacoustic effect through a fiber Bragg grating sensor [12]. However, one potential limitation of this method is its sensitivity to temperature, which can impact the stability of the measurements. Hossain et al. designed a surface plasmon resonance glucose sensor using a graphene mono-layer with controllable optical properties by applying a gate voltage [13]. While SPR fiber optic sensors have ultra-high detection sensitivity, they are challenging to fabricate and calibrate. Currently, most refractive index sensors use optical fiber Mach-Zehnder interferometers (MZI) [16], [17], [18], [19], which require fabricating the optical fiber into a spherical or tapered structure, making them difficult to implement in practical applications. Therefore, a simple and effective fiber interferometer would be of great value. To the best of our knowledge, the study of Michelson interferometer (MI) concentration sensors based on bent fiber has not yet been proposed.

This paper proposed a novel compact fiber-optic Michelson interferometer for measuring solution concentration, which was realized by multiple arc discharge performed on the end of a section of bent bare SMF. To enhance the reliability of the sensor, a neural network demodulation method was introduced to effectively eliminate disturbances caused by dip selection, wavelength sampling rate, and spectral noise.

Compared to previous methods, the proposed sensor system exhibits significant improvements in sensitivity, accuracy, and reliability for concentration measurement.

II. Design and Principle

The fiber optic sensor proposed in this work comprises a bending structure and a terminal arc structure, as illustrated in Fig. 1. The length of the fiber MI sensor is defined as L and the
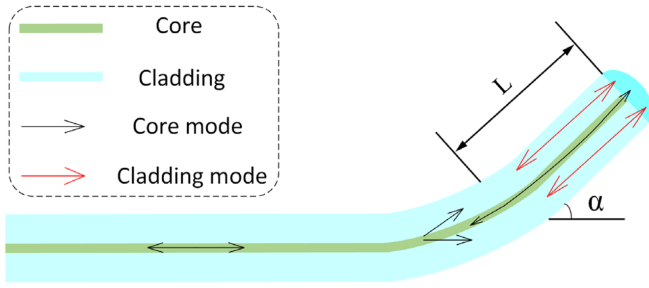
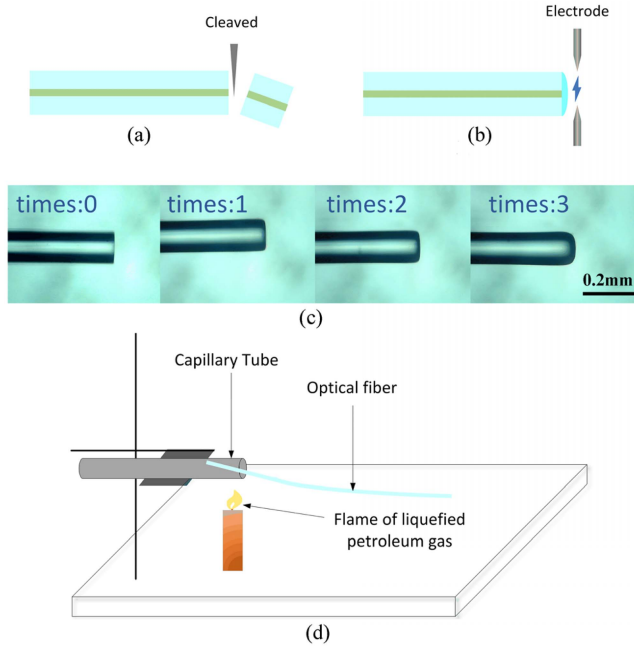Fig. 1.   Structure characteristic diagram of optical fiber sensor.

Fig. 2.   Schematic of the sensor fabrication. (a) Flat cut the fiber end; (b) discharge at the end of fiber; (c) end micrographs of the fiber structure at different discharge times; (d) fabricate the bending structure.

bending angle is α. The bending structure serves as a simple and effective excitation structure, capable of exciting the light in higher-order cladding modes. Meanwhile, the terminal arc structure can cause an obvious optical path difference between the fiber core and cladding.

The whole manufacturing process is illustrated in Fig. 2. The fabrication process was performed by bending a segment of bare SMF and discharging the fiber end. Firstly, take a piece of optical fiber and cut its end flat, as shown in Fig. 2(a). Then an optical fiber fusion splicer (JILONG KL-260C) is used to discharge the optical fiber end with a discharge current of 6 mA and a time of 0.5 seconds as shown in Fig. 2(b). Fiber terminal micrographs under different discharge times are shown in Fig. 2(c). Finally, as shown in Fig. 2(d), the discharged end of the optical fiber was inserted into a silicon tube with an inner diameter of 0.4 mm, and the length of the optical fiber inserted into the silicon tube is L. Since the end of the silicon tube has a supporting force on the optical fiber, the fiber will become bent after being heated by the flame of liquefied petroleum gas. Different bending angles can be obtained by adjusting different heights of the silicon tube.

The whole manufacturing process is simple and no need of fiber fusion operation.

As shown in Fig. 1, part of the light of the fundamental mode will be coupled to the fiber cladding due to the bending and propagates in the cladding as the cladding modes. The light remains in the core and is guided along the fiber. when they reflected back from the arc structure, the cladding modes re-couple with the core mode to construct intermodal interferences at the bending section. The accumulated optical path difference between them will cause the interference at the output end of the fiber, the intensity of reflection spectrum can be expressed as:

$$I_{out} = I_{core} + I_{cladding} + 2\sqrt{I_{core}I_{cladding}} \cos \frac{2\pi}{\lambda}\delta \quad (1)$$

Where I_{core} and $I_{cladding}$ are the light intensity of core mode and cladding modes, respectively. $\frac{2\pi}{\lambda}\delta$ is the phase difference, λ is the wavelength of the incident light. δ is the optical path difference which can be expressed as:

$$\delta = 2L_{eff}\left(n_{eff,co} - n_{eff,cl}\right) \quad (2)$$

Where $n_{eff,co}$ and $n_{eff,cl}$ are the effective refractive index of the core and cladding, respectively. L_{eff} is the effective length of the fiber MI. According to (1), interference dip arises in the reflection spectrum when phase difference is an odd multiple of π:

$$\frac{2\pi}{\lambda_k}\delta = (2k+1)\pi, k = 0, 1, 2, 3\ldots \quad (3)$$

therefore, the wavelength of interference dip λ_{dip} can be written as:

$$\lambda_{dip} = \frac{2\delta}{2k+1} \quad (4)$$

It is seen that the central wavelength of interference dip λ_{dip} is linearly proportional to the refractive index of the solution. The index of solution depends on the concentration by the logarithmic mixing rule [20], which is expressed as follows:

$$\lg n_m = \frac{V_1}{V_1+V_2} \cdot \lg n_1 + \frac{V_2}{V_1+V_2} \cdot \lg n_2 \quad (5)$$

Where V_1 and V_2 are the volumes of solute and solvent before mixing, respectively. n_1 and n_2 refer to the respective indexes of refraction of solute and solvent. The refractive index of the mixed solution is represented by n_m. Then the mass concentration c(n) can be deduced, as shown by the following equation:

$$c(n) = \frac{\rho_1 \ln n_2 - \rho_1 \ln n_m}{(\rho_2 - \rho_1)\ln n_m - (\rho_2 \ln n_1 - \rho_1 \ln n_2)} \quad (6)$$

Where ρ_1 and ρ_2 are the densities of the solute and solvent, respectively. Thus, concentration can be measured by monitoring the wavelength shift of the reflective resonant spectrum λ_{dip}.

Because the bending angle α of the fiber is an important structural parameter of the proposed MI sensor, the optical field distributions of the MI sensor with the change of bending angle were simulated based on the Beam Propagation Method (BPM) as shown in Fig. 4. The Rsoft software is applied to implement the simulation. In the simulation, the diameter of core and cladding were set as 8.25 μm and 125 μm, respectively. The
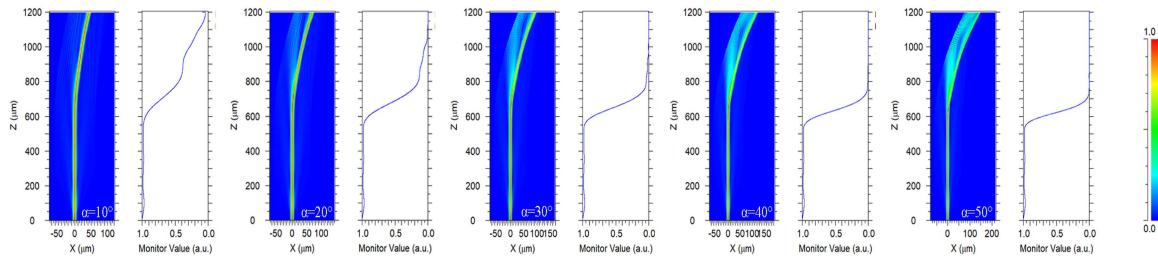
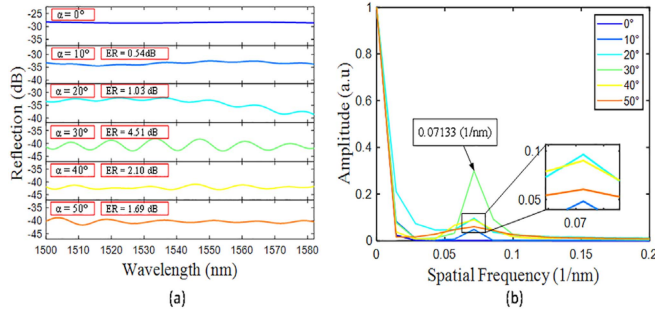Fig. 3. Light field simulation diagrams of bending structure with different bend angle.

Fig. 4. (a) Reflection spectra with different bending angles. (b) Spatial frequency spectra with different bending angles.
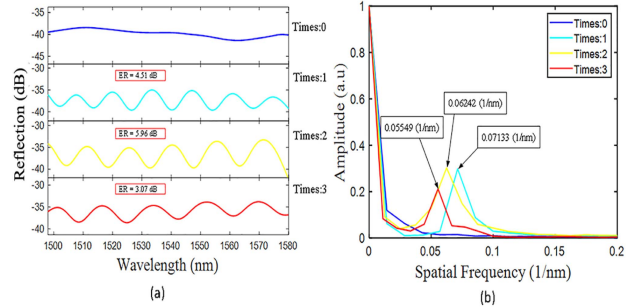

Fig. 5. (a) Sensor reflection spectra at various discharge times (b) the corresponding spatial frequency at various discharge times.
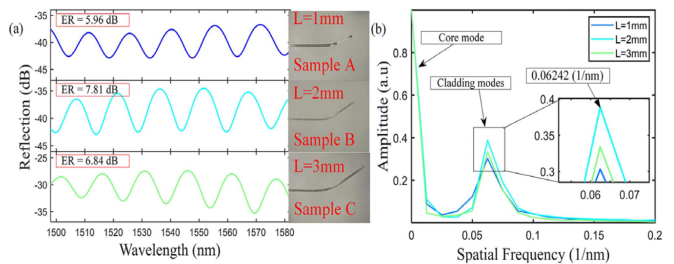

Fig. 6. (a) Reflection spectra of the sensor at different L. (b) The corresponding spatial frequency of the spectrum at different L.

refractive index of fiber core and cladding was set as 1.4504 and 1.4447 [21], respectively. Bending angle increased from 10° to 50° in steps of 10° and the simulation results were plotted in Fig. 4. Light gradually travels out of the core to the cladding as the bending angle increases. When the angle is equal to 40°, there is an excess of light travels to the cladding, resulting in a light intensity imbalance between the core and cladding and lowering the extinction ratio (ER). Based on these results, it can be preliminarily determined that the appropriate bending angle was about 30°.

To determine the optimal parameters of the sensor, experimental tests were conducted to observe the effect of sensor parameters on the reflection spectrum. First, the number of discharges at the end of the fiber was kept constant, and the sensor length was set to 1 mm. Reflection spectra with different bending angles were obtained, as shown in Fig. 4(a). At a bending angle of 20°, the reflection spectrum exhibited clear peaks. As the angle increased from 0° to 50° in steps of 10°, the ER of the reflection spectrum increased at first and subsequently declined. The ER reached a maximum at an angle of 30°. Fig. 4(b) is the fast Fourier transform (FFT) corresponding to the spectrum in Fig. 4(a). Notably, the spatial frequency remained relatively constant in the FFT plot, and the inverse of the spatial frequency represented the free spectral range (FSR) of the reflection spectrum.

That is to say, the FSR of the reflected spectrum is independent of the bending angle.

Through the simulations and experimental testing described above, an appropriate bending angle of around 30° was determined. The terminal arc structure is a crucial component of the fiber MI sensor, and it is therefore necessary to study the influence of the terminal arc structure on the reflection spectrum

under different discharge times. During the experimental tests, the bending angle and sensor length remained constant at 30° and 1 mm, respectively. By comparing the reflection spectra at different discharge times, it was observed that the extinction ratio of the reflection spectrum initially increased and subsequently decreased with increasing discharge times, as shown in Fig. 5(a). The maximum ER was obtained when the discharge times were 2 times. Fig. 5(b) displayed the sensor spatial frequency spectra at various discharge times. The spatial frequency of the sensor decreased as the number of discharges increased, as shown in Fig. 5(b). Therefore, the discharge times had an impact on the FSR of the reflection spectrum.

Based on the above analysis, the optimal bending angle and discharge times were 30° and 2 times, respectively. With these fiber manufacturing parameters, three fiber optic sample sensors with different lengths were made: Samples A, B, and C, with lengths of 1 mm, 2 mm, and 3 mm, respectively. When the bending angle and discharge times were kept constant, the extinction ratio of reflected spectrum would change slightly with the change of fiber length as shown in Fig. 6(a). Fig. 6(b) illustrated that the
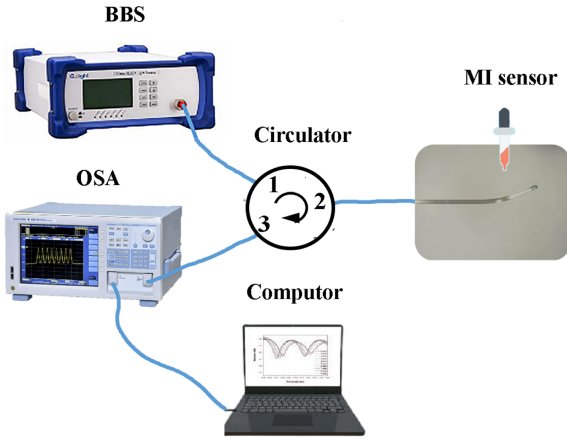
Fig. 7. Schematic diagram of experimental setup.

Fig. 8. (a) Interference spectra of glycerol solution under different concentrations. (b) 6 dips' wavelength shift versus concentrations increase.

FSR of the sensors at different lengths was almost unchanged. Combined with the previous analysis, it could be concluded that FSR was mainly determined by the discharge times at the fiber end. In addition, considering the terminal arc structure would be submerged by the solution dropped on the bending region if the fiber length was too short, Eventually, the fiber MI sensor with a length L of 3 mm was chosen for subsequent experiments.

III. EXPERIMENTAL RESULTS AND DISCUSSION

The experimental scheme was illustrated in Fig. 7. The incident light was transmitted from the broadband light source (BBS) to the port 1 of the circulator and through the port 2 of the circulator to the fiber MI sensor. The reflected light was transmitted to the optical spectrum analyzer (OSA, Yokogawa, AQ6370D) through the port 3 of circulator. The reflection spectra at different concentrations were recorded by OSA.

Glycerol was selected for the experiment due to its high water solubility. Glycerol solution with concentration range of 5~80% (interval of 5%) was prepared. The solution was added dropwise to the bending region with a rubber-tipped dropper. Before each measurement, the bending region was flushed with deionized water and blown dry. The interference spectra of wavelength shift in the different glycerol concentration solutions were given in Fig. 8(a). As we can see from Fig. 8(a) that the red shift of the interference spectrum becomes more significant with the concentration increases, and the pattern of interference almost remains the same.

Due to the presence of multiple unknown variables, calculating the solution concentration using (4) and (6) can be challenging. To quantitatively link the dips' response to external change of glycerol solution concentration, a regression analyses were performed. To facilitate easy comparison of sensitivity differences among dips, we forced the starting point of the best fitting lines to be zero by subtracting its starting value from each of fitting values.

The nonlinear relationship between glycerol solution concentration and the central wavelength shifts of all dips can be observed in Fig. 8(b). the sensitivities of different dips were quite
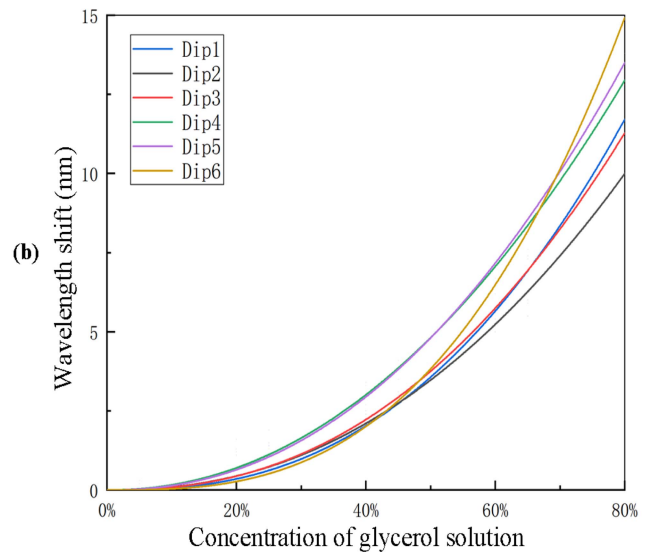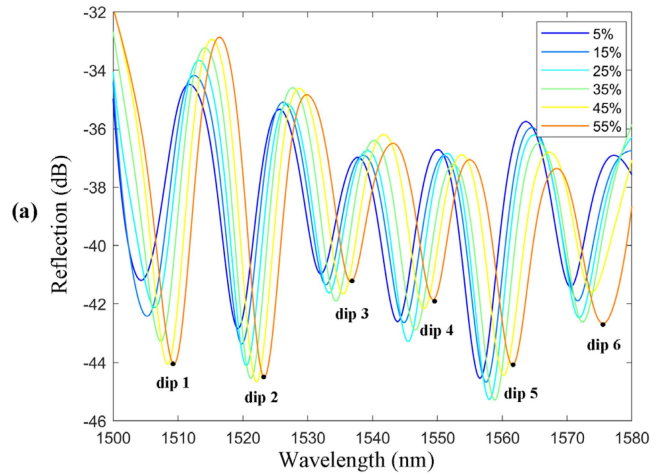
similar but numerical differences were obvious. So, the sensitivity of the proposed structure is dip-dependent. Meanwhile, the resonant valley wavelength was determined by searching the minimum intensity value in a certain wavelength window, the results may be affected by wavelength sampling rate or spectral noise.

It is worth noting that nonlinear variations in the data may result in inaccurate concentration extrapolation when using fitted curves, and the use of higher order fitting curves could lead to overfitting. Moreover, the wavelength tracking technology used to search the dip wavelength relies only on one sampling point, which could be affected by the wavelength sampling rate or spectral noise, ultimately impacting its accuracy [21]. The measurement error caused by either wavelength sampling or spectral noise was totally random and unpredictable.

Thus, in order to improve the stability and accuracy, machine learning based on LSTM was employed for glycerol concentration demodulation [22]. Unlike traditional recurrent neural networks (RNNs), LSTM utilizes memory cells to filter redundant information, which can more efficiently extract valuable
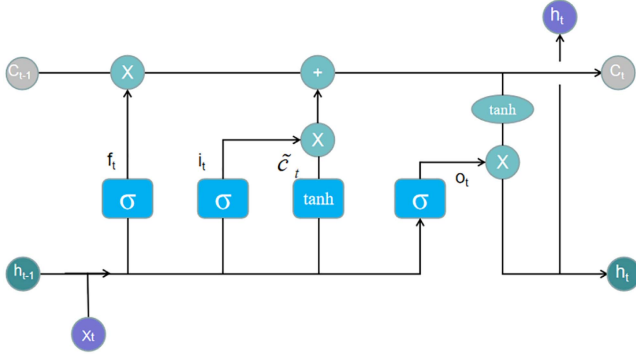
Fig. 9. Typical structure of a single LSTM cell.

Fig. 10. (a) The RMSE and loss function curves in the training process. (b) Comparison of actual concentration and LSTM predicted concentration.

information from spectral data with high redundancy. A typical LSTM neural network cell is configured mainly by three gates: input gate, forget gate and output gate. The input gate processes newly arriving data, while the forget gate determines the optimal time lag for the input sequence by selectively discarding previous results. The output gate aggregates all results to generate the LSTM cell output. By utilizing these three control gates, the memory capacity of the network model is increased, allowing for improved accuracy in concentration measurement by capturing the correlation of spectral data. The typical structure of LSTM cells is shown in Fig. 9.

Where h_{t-1} and X_t represent output of last LSTM unit and current input, respectively. C_{t-1} represents the memory from last LSTM unit. The updated cell state C_t is determined by the results of the previous forget gate and input gate. The final output result h_t is obtained by multiplying the updated cell state with the output gate. The calculation formula is shown as (7) and (8).

$$C_t = \sigma(W_f \cdot [h_{t-1}, X_t] + b_f) * C_{t-1}$$
$$+ \sigma(W_i \cdot [h_{t-1}, X_t] + b_i)$$
$$* \tanh(W_C \cdot [h_{t-1}, X_t] + b_c) \tag{7}$$
$$h_t = \sigma(W_o * [h_{t-1}, X_t] + b_o) * \tanh(C_t) \tag{8}$$

In this study, 17 spectra data corresponding to glycerol solutions with different concentrations were selected as training samples. Each sample contained 800 data points within the wavelength range of 1500–1580 nm. Due to limitations in the sample sources, Bootstrap resampling was utilized to expand the sampling set. Bootstrap resampling was originally proposed by Professor Efron, which is essentially a non-parametric resampling method that does not require assumptions about the sampling data [23]. During the sampling process, samples have a probability of approximately 36.8% of not being selected. In this case, the unsampled samples can be used as the test set, while the remaining samples can be used to train the neural network. Afterward, the network was trained for 200 epochs with a batch size of 4. The training strategy employed the random gradient descent method along with the mean absolute error (L1) loss function.
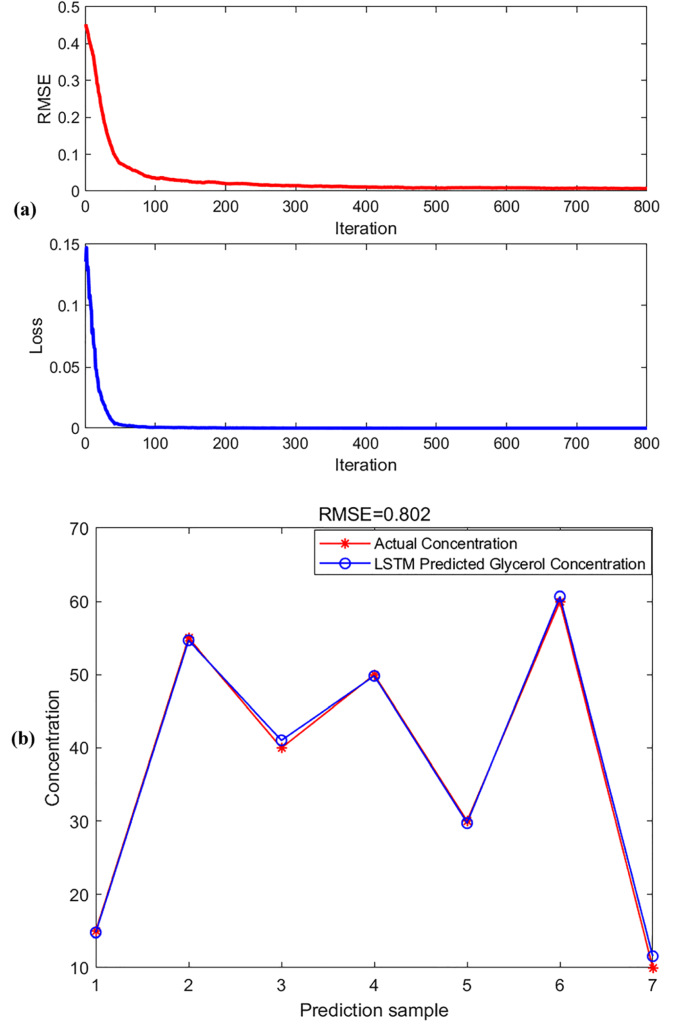
Fig. 10(a) displayed the training performance curves, which indicated that the error and loss gradually decreased and eventually stabilized. To further evaluate the model performance, the data from the test set were fed into the trained model for concentration prediction. The prediction results were shown in Fig. 10(b), which demonstrated that the predicted concentrations were generally consistent with the actual values. The root mean square error (RMSE) was 0.802, and the prediction accuracy reached 97.5%, indicating that the spectral information can be effectively used to predict the concentration of glycerol solutions using a well-trained LSTM neural network. Furthermore, this demodulation method can be applied to measure the concentrations of other solution concentration by adjusting the sampling range of wavelengths and the number of LSTM neural network layers.

IV. CONCLUSION

In this paper, a novel compact optical fiber concentration sensing system based on machine learning demodulation was proposed. The sensor consisted of a bending structure and a

terminal arc structure. Simulation and experimental testing were carried out to determine the bending angle α of the fiber as 30°. By comparing the extinction ratio of reflection spectra at different discharge times and lengths, the optimal discharge times and lengths were set to 2 times and 3 mm, respectively. In the experiments, glycerol solutions with different concentrations ranging from 5% to 80% were used to test the sensors. As the concentration increased, the interference spectrum exhibited a significant red shift. Machine learning based on long short-term memory (LSTM) was employed to demodulate and the accuracy of the predictions reached 97.5%. The experiments demonstrated that the proposed method is more stable and accurate than conventional peak wavelength tracking because LSTM can avoid the effects of dip selection, wavelength sampling rate and spectral noise on the peak wavelength tracking. Moreover, the proposed sensor system exhibited the advantages of compact size, low cost, high robustness, and convenient fabrication, and had the potential for applications in the fields of medicine, biology, chemistry, and environmental concentration monitoring.

REFERENCES

[1] N. A. Mostafa, A. M. Tayeb, O. A. Mohamed, and R. Farouq, "Biodegradation of petroleum oil effluents and production of biosurfactants: Effect of initial oil concentration," *J. Surfactants Detergents*, vol. 22, no. 2, pp. 385–394, 2019.

[2] P. Remor, J. Bastos, J. Alino, L. Frare, P. Kaparaju, and T. Edwiges, "Optimization of chemical solution concentration and exposure time in the alkaline pretreatment applied to sugarcane bagasse for methane production," *Environ. Technol.*, vol. 44, no. 19, pp. 2843–2855, 2023.

[3] L. Wu et al., "Morphology, structure and corrosion resistance of Mg–Al LDH films fabricated in different Al 3+ concentration solutions," *Rare Met.*, vol. 42, no. 2, pp. 697–704, 2023.

[4] B. Li, H. Liu, M. Amin, L. A. Wegiel, L. S. Taylor, and K. J. Edgar, "Enhancement of naringenin solution concentration by solid dispersion in cellulose derivative matrices," *Cellulose*, vol. 20, pp. 2137–2149, 2013.

[5] I. Y. Yanina, A. P. Popov, A. V. Bykov, I. V. Meglinski, and V. V. Tuchin, "Monitoring of temperature-mediated phase transitions of adipose tissue by combined optical coherence tomography and Abbe refractometry," *J. Biomed. Opt.*, vol. 23, no. 1, 2018, Art. no. 016003.

[6] R. J. McNichols and G. L. Cote, "Optical glucose sensing in biological fluids: An overview," *J. Biomed. Opt.*, vol. 5, no. 1, pp. 5–16, 2000.

[7] W. Chen, C. Zhao, B. Mao, H. Chen, and C. Shen, "Detection of aflatoxin B_1 in food based on SMF taper combined with fiber loop ring down technique," *IEEE Sensors J.*, vol. 20, no. 5, pp. 2446–2451, Mar. 2020.

[8] M. A. Butt, G. S. Voronkov, E. P. Grakhova, R. V. Kutluyarov, N. L. Kazanskiy, and S. N. Khonina, "Environmental monitoring: A comprehensive review on optical waveguide and fiber-based sensors," *Biosensors*, vol. 12, no. 11, 2022, Art. no. 1038.

[9] G. Keiser, F. Xiong, Y. Cui, and P. P. Shum, "Review of diverse optical fibers used in biomedical research and clinical practice," *J. Biomed. Opt.*, vol. 19, no. 8, 2014, Art. no. 080902.

[10] H. Mohammed and M. Yaacob, "A novel modified fiber Bragg grating (FBG) based ammonia sensor coated with polyaniline/graphite nanofibers nanocomposites," *Opt. Fiber Technol.*, vol. 58, 2020, Art. no. 102282.

[11] Y. Zhao, L. Cai, X.-G. Li, and F.-C. Meng, "Liquid concentration measurement based on SMS fiber sensor with temperature compensation using an FBG," *Sensors Actuators B: Chem.*, vol. 196, pp. 518–524, 2014.

[12] M. Rong and L.-S. Zhang, "Liquid concentration measurement based on the optoacoustic effect and fiber Bragg grating sensor technology," *Opt. Eng.*, vol. 45, no. 4, 2006, Art. no. 040501.

[13] M. M. Hossain and M. A. Talukder, "Gate-controlled graphene surface plasmon resonance glucose sensor," *Opt. Commun.*, vol. 493, 2021, Art. no. 126994.

[14] B. Li et al., "No-core optical fiber sensor based on surface plasmon resonance for glucose solution concentration and temperature measurement," *Opt. Exp.*, vol. 29, no. 9, pp. 12930–12940, 2021.

[15] S. Wu, Q. Tan, E. Forsberg, S. Hu, and S. He, "In-situ dual-channel surface plasmon resonance fiber sensor for temperature-compensated detection of glucose concentration," *Opt. Exp.*, vol. 28, no. 14, pp. 21046–21061, 2020.

[16] Z. Pan, J. Feng, X. Hu, C. Jia, and X. Huang, "High sensitivity fiber sensor for measurement of Cd^{2+} concentration in aqueous solution based on reflective Mach-Zehnder interference with temperature calibration," *Opt. Exp.*, vol. 27, no. 22, pp. 32621–32629, 2019.

[17] C. Liao, F. Zhu, P. Zhou, and Y. Wang, "Fiber taper-based Mach–Zehnder interferometer for ethanol concentration measurement," *Micromachines*, vol. 10, no. 11, 2019, Art. no. 741.

[18] F. Wang, H. Lu, X. Wang, and Y. Liu, "Measurement of concentration and temperature using a fiber loop ring-down technique with core-offset structure," *Opt. Commun.*, vol. 410, pp. 13–16, 2018.

[19] Y.-L. Fang, C.-T. Wang, and C.-C. Chiang, "A small U-shaped bending-induced interference optical fiber sensor for the measurement of glucose solutions," *Sensors*, vol. 16, no. 9, 2016, Art. no. 1460.

[20] Y. Wu, X. Zhao, F. Li, and Z. Fan, "Evaluation of mixing rules for dielectric constants of composite dielectrics by MC-FEM calculation on 3D cubic lattice," *J. Electroceramics*, vol. 11, pp. 227–239, 2003.

[21] X. Fu, P. Lu, W. Ni, H. Liao, D. Liu, and J. Zhang, "Phase demodulation of interferometric fiber sensor based on fast Fourier analysis," *Opt. Exp.*, vol. 25, no. 18, pp. 21094–21106, 2017.

[22] Y. Yu, X. Si, C. Hu, and J. Zhang, "A review of recurrent neural networks: LSTM cells and network architectures," *Neural Comput.*, vol. 31, no. 7, pp. 1235–1270, 2019.

[23] A. K. Dwivedi, I. Mallawaarachchi, and L. A. Alvarado, "Analysis of small sample size studies using nonparametric bootstrap test with pooled resampling method," *Statist. Med.*, vol. 36, no. 14, pp. 2187–2205, 2017.